Analytical solutions of the potential vorticity invertibility principle

Matthew T. Masarik[1] and Wayne H. Schubert[1]

Received 17 August 2012; revised 20 December 2012; accepted 27 December 2012 ; published 11 June 2013.

[1] We define the *f*-plane, *y*-independent, potential vorticity (PV) invertibility principle as a coupled pair of first-order partial differential equations relating the balanced wind and mass fields to the known PV. Analytical solutions of this invertibility principle are derived for cases in which an isolated PV anomaly is confined within a region of the vertical plane. The solutions aid in understanding the dynamics of low-latitude PV intrusions whose associated cloud patterns are often referred to as cloud surges, or moisture bursts, and whose flow patterns are often referred to as tropical upper tropospheric troughs. The existence of such tongues of high PV air intruding into the upper troposphere is documented using reanalysis data from the "Year" of Tropical Convection data set. The solutions illustrate the phenomenon of isentropic upglide below an upper tropospheric positive anomaly in PV. They also quantify how the partitioning of PV between absolute vorticity and static stability depends on the shape and strength of the PV anomaly. With slight modifications, the solutions apply to the problem of determining the balanced flow induced by a surface temperature anomaly, which is equivalent to a very thin layer of infinite PV at the surface. Through numerical solutions of the fully nonlinear invertibility principle we provide justification for the anelastic-type approximation used in the analytical theory.

Citation: Masarik, M. T., and W. H. Schubert (2013), Analytical solutions of the potential vorticity invertibility principle, *J. Adv. Model. Earth Syst.*, *5*, 366–381, doi:10.1002/jame.20011.

1. Introduction

[2] In the boreal fall, winter, and spring the upper troposphere in the eastern Pacific differs from most of the tropical belt in the sense that it contains westerly rather than easterly winds. This background westerly flow is favorable for the equatorward propagation of midlatitude Rossby waves [*Webster and Holton*, 1982; *Hoskins and Ambrizzi*, 1993; *Tomas and Webster*, 1994]. Climatologies of the intrusions of extratropical air into the tropical upper troposphere have been produced by *Iskenderian* [1995], *Postel and Hitchman* [1999], *Waugh and Polvani* [2000], and *Waugh and Funatsu* [2003]. These studies show that in the eastern Pacific such events produce narrow tongues of high potential vorticity (PV) that have an almost north–south orientation and last for several days. Most of these PV structures extend up into the lower stratosphere but only a small percentage penetrate deeply downward. A phase-shifted (i.e., each trough line shifted to 140°W) composite of 103 cases has been produced by *Waugh and Funatsu* [2003] and is shown in Figure 1, which hints that such Rossby wave breaking can be enhanced by steep PV gradients found upstream [*Scott et al.*, 2004]. Low-latitude PV intrusions are also important in understanding many other aspects of tropical dynamics, such as stratosphere-troposphere exchange [*Holton et al.*, 1995; *Juckes*, 1999; *Scott et al.*, 2001], the structure of the tropical tropopause [*Gettelman and Birner*, 2007; *Gettelman et al.*, 2009; *Fueglistaler et al.*, 2009], and the distributions of humidity, cloud, and ozone [*Kiladis and Weickmann*, 1992; *Kiladis*, 1998; *Juckes and Smith*, 2000; *Hoskins et al.*, 2003; *Waugh*, 2005; *Kley et al.*, 2007; *Funatsu and Waugh*, 2008].

[3] An example of a low-latitude PV intrusion occurred in January 2009, during an intensive data analysis period called the "Year" of Tropical Convection (YOTC). The YOTC data set consists of 2 years of European Centre for Medium-Range Weather Forecasts reanalysis fields from 1 May 2008 to 30 April 2010. Because PV intrusions can be as narrow as 200 km [*Appenzeller and Davies*, 1992], data with high horizontal resolution is needed. The YOTC data are available on a latitude/longitude grid having 0.25° × 0.25° resolution and on 15 pressure levels between the surface and 100 hPa. The PV intrusion event started around 10 January 2009 and lasted nearly a week. The time series for this event is shown in Figure 2. At 0000 UT on 10 January 2009, a wave in the 250 hPa PV field is starting to develop near the date line and 30°N. Over the next 36 h the intrusion pushes southward and has

[1]Department of Atmospheric Science, Colorado State University, Fort Collins, Colorado, USA.

1942-2466/13/1002/jame.20011

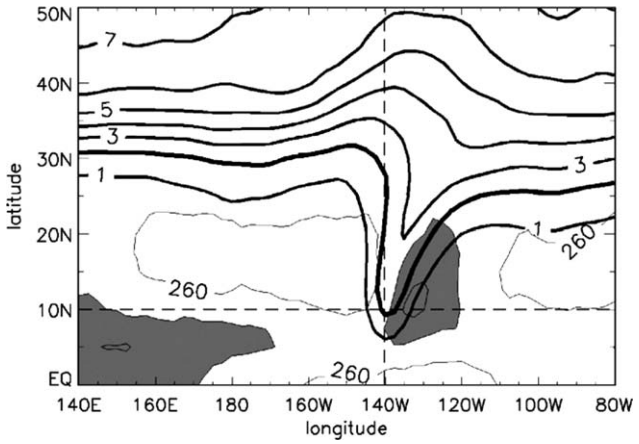

Figure 1. Composite low-latitude PV intrusion (the thick PV contours are labeled in PVU) over the North Pacific on the 350 K isentropic surface. Thin contours show the outgoing longwave radiation, with the shaded regions indicating values less than 240 W m^{-2}, which is typical of tropical convection. The tropical convection just east of the high PV intrusion is associated with the isentropic upglide process. Adapted from *Waugh and Funatsu* [2003]. Copyright by American Meteorological Society, and used with permission.

elevated values of PV at its tip, between 15°N and 20°N. During this time the Hawaiian Islands experienced a Kona storm, bringing heavy rain and westerly winds where the northeast trades normally prevail. At 0000 UT on 12 January 2009, the intrusion starts to weaken and become a filament, and by 1200 UT a vortex is seen to have developed within the filament just north of Hawaii. These "subfilament" scale structures were identified by *Scott et al.* [2001] and studied via a nonhydrostatic mesoscale model as well as the technique of contour advection with surgery, developed by *Dritschel* [1989]. The mesoscale structure of filaments was also discussed by *Appenzeller et al.* [1996], who produced a schematic of archetypal PV streamer patterns. According to their classification, the intrusion described here can be identified as a Type II streamer (i.e., a streamer with a north–south orientation), with the remnants of a decaying intrusion to the east being a Type I streamer (i.e., a streamer that arches around the neighboring anticyclone to form an elongated band of high PV with a northeast–southwest orientation). During the next 2 days the intrusion continues to stretch out along its axis, reaching as low as 10°N. At 1200 UT on 16 January 2009 (not shown, but further discussion can be found in *Masarik* [2012]), the filament starts to strengthen and grow slightly in width, maintaining its north–south orientation while moving eastward and making landfall on the west coast of North America.

[4] A vertical cross section of this event, early in its development at 0600 UT on 11 January 2009, is shown in Figure 3. Figure 3 (top) shows the intrusion with its tip at 20°N and having values near 7–8 potential vorticity units (PVU) along much of its length. The heavy black line indicates the location of the cross section taken at 30°N from 180°W to 150°W. Figure 3 (bottom) shows a vertical cross section of PV, meridional wind, and potential temperature. There is a region of anomalously high PV protruding downward into the troposphere, reaching as far as 600 hPa with approximately 2 PVU and having values of 7–8 PVU in its core. Flanking the sides of the anomaly are jets which have a high degree of symmetry in both shape and magnitude. These circulation anomalies reach their maximum on the edges of the PV anomaly. On the right side the northward velocity has a maximum of 60 m s^{-1} and on the left side a small core reaches a minimum of -70 m s^{-1}. Underneath the anomaly the surfaces of potential temperature are drawn upward, which is seen most easily in the 300 and 310 K isentropes.

[5] The goal of the present work is to better understand the dynamics of such PV intrusions through the derivation of simple analytical solutions of the PV invertibility principle. This paper is organized as follows. The invertibility principle in isentropic coordinates is derived in section 2. Section 3 presents simple analytical solutions of this invertibility principle for both thin and thick lenses of PV in the upper troposphere. Section 4 shows how the analytical solutions also apply to the problem of surface temperature gradients or equivalently the problem of infinite PV in a very thin layer at the surface. Section 5 presents numerical solutions of the invertibility principle and discusses the effects of the anelastic-type density approximation that is used in the derivation of the analytical solutions. Concluding remarks are given in section 6.

2. Invertibility Principle in Terms of Cauchy-Riemann Conditions

[6] Consider a dry, geostrophically balanced flow that is entirely in the y direction. Using potential temperature θ as the vertical coordinate and denoting the y component of the flow by $v(x,\theta)$, the PV for the y-independent flow on an f-plane is denoted $P(x,\theta)$ and given by

$$P=\left(f+\frac{\partial v}{\partial x}\right)\left(-\frac{1}{g}\frac{\partial p}{\partial \theta}\right)^{-1}, \tag{1}$$

where f is the constant Coriolis parameter, g is the acceleration of gravity, and $p(x,\theta)$ is the pressure. The domain is considered infinite in x, but with wind field and mass field anomalies localized near the origin, so that $v \to 0$ and $p \to \tilde{p}(\theta)$ as $x \to \pm\infty$, where $\tilde{p}(\theta)$ is the specified far-field vertical profile of pressure. In the far-field the vertical profile of PV is denoted $\tilde{P}(\theta)$ and given by

$$\tilde{P}=f\left(-\frac{1}{g}\frac{\partial \tilde{p}}{\partial \theta}\right)^{-1}. \tag{2}$$

Defining the Exner function by $\Pi(p)=c_p(p/p_0)^{\kappa}$ and denoting the density by $\rho(x,\theta)$ and the far-field density by $\tilde{\rho}(\theta)$, it is easily shown that $\theta\rho(d\Pi/dp)=1$ and

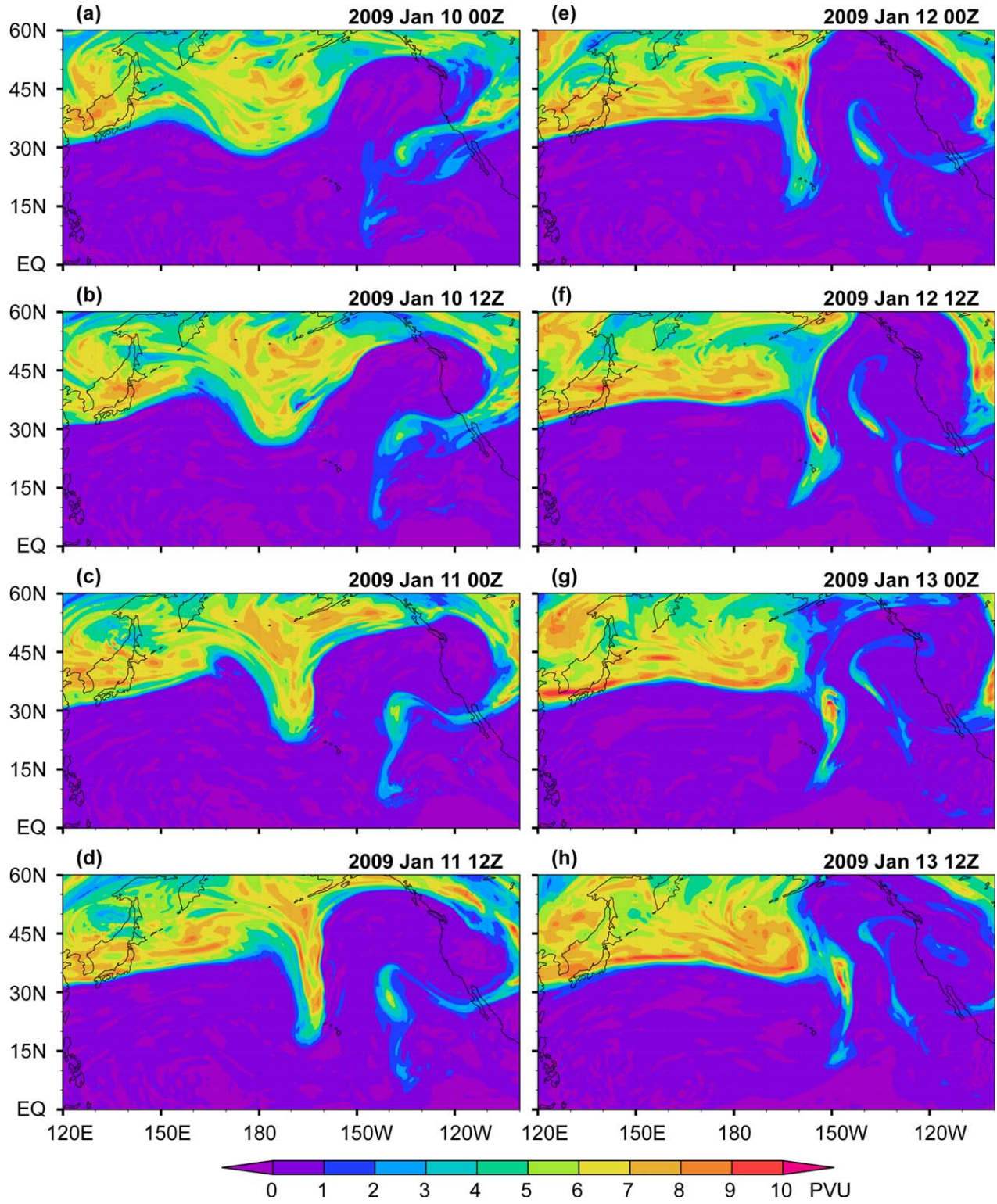

Figure 2. Time series of PV on the 250 hPa surface, shown every 12 h starting at 0000 UT on 10 January 2009. The color bar at the bottom indicates the values of PV in PVU.

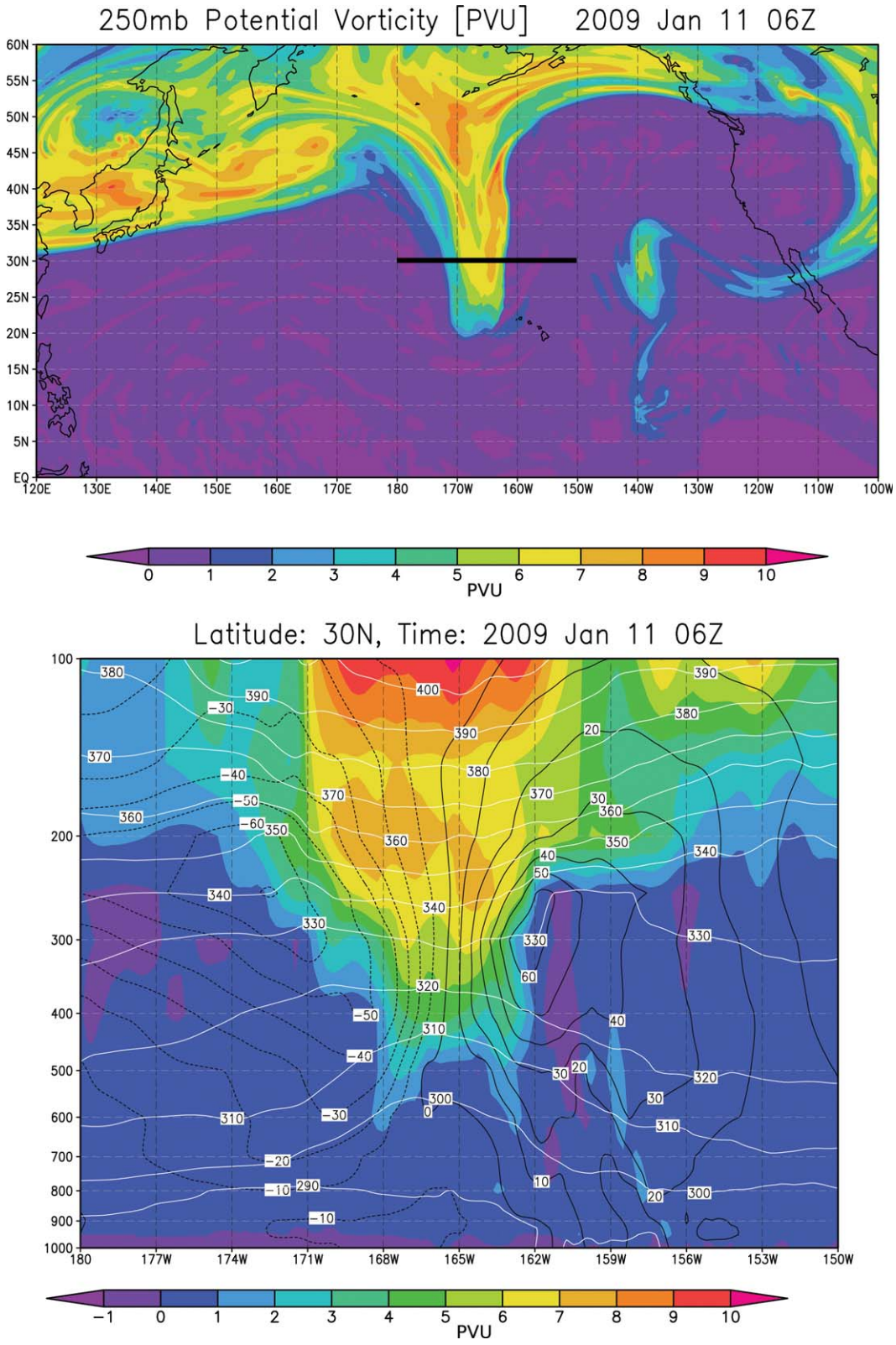

Figure 3. A high PV intrusion in an early stage. (top) PV on the 250 hPa surface at 0600 UT on 11 January 2009. The thick black line indicates the location of the vertical cross section shown in the lower panel. (bottom) PV (colors), meridional velocity v (solid and dashed black lines every 10 m s^{-1}), and potential temperature θ (white lines every 10 K). The color bars indicate the PV values in PVU.

$\theta\tilde{\rho}\left(\mathrm{d}\tilde{\Pi}/\mathrm{d}\tilde{p}\right)=1$, which allows the ratio of equations (1) and (2) to be written in the form

$$\begin{aligned} f\frac{P}{\tilde{P}} &= \left(f+\frac{\partial v}{\partial x}\right)\left(\frac{\partial\tilde{p}/\partial\theta}{\partial p/\partial\theta}\right) \\ &= \left(f+\frac{\partial v}{\partial x}\right)\left(\frac{\tilde{\rho}\left(\mathrm{d}\tilde{\Pi}/\mathrm{d}\tilde{p}\right)(\partial\tilde{p}/\partial\theta)}{\rho(\mathrm{d}\Pi/\mathrm{d}p)(\partial p/\partial\theta)}\right) \\ &= \left(f+\frac{\partial v}{\partial x}\right)\left(\frac{\tilde{\rho}\left(\partial\tilde{\Pi}/\partial\theta\right)}{\rho(\partial\Pi/\partial\theta)}\right). \end{aligned} \tag{3}$$

Equation (3) can also be written in the form

$$\frac{\partial(v+fx)}{\partial x}+\left(\frac{\theta_c^2N^2f\rho P}{g^2\tilde{\rho}\tilde{P}}\right)\frac{\partial\Pi}{\partial\theta}=0, \tag{4}$$

where we have defined the far-field buoyancy frequency $N(\theta)$ by

$$N^2(\theta)=\frac{g^2}{\theta_c^2}\left(-\frac{\mathrm{d}\tilde{\Pi}}{\mathrm{d}\theta}\right)^{-1}, \tag{5}$$

with the constant θ_c denoting the center of the PV anomaly. For simplicity we hereafter assume that the buoyancy frequency N is a constant, so that integration of equation (5) yields

$$\tilde{\Pi}(\theta)=\Pi_c-\frac{g^2}{\theta_c^2N^2}(\theta-\theta_c), \tag{6}$$

where the constant Π_c denotes the far-field value of the Exner function at $\theta=\theta_c$. Because of the relation $\rho=[p_0/(R\theta)]\left(\Pi/c_p\right)^{(1-\kappa)/\kappa}$, the factor $(\rho/\tilde{\rho})$ in equation (4) represents a weak nonlinear effect. In the analytical solutions of sections 3 and 4 we shall ignore this weak nonlinear effect by making the approximation $(\rho/\tilde{\rho})=1$. In the numerical solutions of section 5 this nonlinearity will be retained.

[7] Equation (4) and the thermal wind relation can now be written in the form

$$\frac{\partial(v+fx)}{\partial x}+\frac{\theta_c^2N^2fP}{g^2\tilde{P}}\frac{\partial\Pi}{\partial\theta}=0, \tag{7}$$

$$\frac{\partial(v+fx)}{\partial\theta}-\frac{1}{f}\frac{\partial\Pi}{\partial x}=0. \tag{8}$$

We conclude that the governing equations of the invertibility principle are the Cauchy-Riemann conditions (7) and (8), which constitute a system of first-order partial differential equations for $v(x,\theta)$ and $\Pi(x,\theta)$ given $P(x,\theta)$. It is also possible to eliminate Π between equations (7) and (8) to obtain a second-order elliptic equation for v or to eliminate v to obtain a similar second-order elliptic equation for Π. However, since section 3 involves P fields that are discontinuous, it proves more convenient to work with the first-order equations (7) and (8).

3. Solution of the Invertibility Principle

[8] In this section we consider PV fields given by

$$\frac{P}{\tilde{P}}=\begin{cases}\gamma & \text{if } \left(\frac{x}{a}\right)^2+\left(\frac{g(\theta-\theta_c)}{\theta_cNfb}\right)^2<1,\\ 1 & \text{if } \left(\frac{x}{a}\right)^2+\left(\frac{g(\theta-\theta_c)}{\theta_cNfb}\right)^2>1,\end{cases} \tag{9}$$

where the constant γ specifies the strength of the PV anomaly within the elliptical patch whose center is at $(x,\theta)=(0,\theta_c)$ and whose shape is specified by the constants a and b. To solve the invertibility problem for the PV distribution given in equation (9) we must solve equations (7) and (8) inside the ellipse with $P/\tilde{P}$ replaced by the constant γ, then solve equations (7) and (8) outside the ellipse with $P/\tilde{P}$ replaced by unity, and finally match the solutions for v and Π along the ellipse. To derive the solutions of equations (7) and (8) in the outer region, it is convenient to use the elliptic coordinates (ϱ,φ), defined by

$$\left\{\begin{aligned} x+i\left(\frac{g(\theta-\theta_c)}{\theta_cNf}\right) &= c\,\cosh(\varrho+i\varphi)\\ x &= c\,\cosh\,\varrho\,\cos\varphi\\ \frac{g(\theta-\theta_c)}{\theta_cNf} &= c\,\sinh\,\varrho\,\sin\varphi\\ c &= (a^2-b^2)^{1/2}\end{aligned}\right\} \tag{10}$$

if $a>b$ (thin lens), or by

$$\left\{\begin{aligned} x+i\left(\frac{g(\theta-\theta_c)}{\theta_cNf}\right) &= c\,\sinh(\varrho+i\varphi)\\ x &= c\,\sinh\,\varrho\,\cos\,\varphi\\ \frac{g(\theta-\theta_c)}{\theta_cNf} &= c\,\cosh\,\varrho\,\sin\,\varphi\\ c &= (b^2-a^2)^{1/2}\end{aligned}\right\} \tag{11}$$

if $a<b$ (thick lens). Note that the top line in each grouping is simply the complex form of the middle two lines in the grouping. The elliptic coordinate lines form a system of ellipses and hyperbolas. For example, for the thin lens case, it is easily shown that

$$\frac{x^2}{c^2\,\cosh^2\,\varrho}+\frac{\left[g(\theta-\theta_c)/(\theta_cNf)\right]^2}{c^2\,\sinh^2\,\varrho}=1, \tag{12}$$

and

$$\frac{x^2}{c^2\,\cos^2\,\varphi}-\frac{\left[g(\theta-\theta_c)/(\theta_cNf)\right]^2}{c^2\,\sin^2\,\varphi}=1, \tag{13}$$

so that the lines of constant ϱ are ellipses and the lines of constant φ are hyperbolas (see Figure 4). The complete family of ellipses is generated by allowing the coordinate ϱ to vary over the range $0 \le \varrho < \infty$, while the complete family of hyperbolas is generated by allowing the coordinate φ to vary over the range $0 \le \varphi \le 2\pi$. In particular, the ellipse $(x/a)^2+[g(\theta-\theta_c)/(\theta_c N f b)]^2=1$, which just encloses the region of anomalous PV, is specified by $\varrho=\varrho_0=\tanh^{-1}(b/a) = \frac{1}{2}\ln[(a+b)/(a-b)]$. As ϱ becomes very large, $\cosh\varrho \approx \sinh\varrho \approx \frac{1}{2}e^{\varrho}$, so that the lines of constant ϱ approach circles with radius $\frac{1}{2}ce^{\varrho}$, and the lines of constant φ approach the straight radials $\varphi=\tan^{-1}[g(\theta-\theta_c)/(\theta_c N f x)]$.

[9] Inside the ellipse $\varrho=\varrho_0$, the Cauchy-Riemann equations are now equations (7) and (8), with $P/\tilde{P}$ replaced by the constant γ. Outside this ellipse the Cauchy-Riemann equations are now equations (7) and (8), with $P/\tilde{P}$ replaced by unity, and with the resulting equations transformed to elliptic coordinates. Thus, the detailed statement of the problem is

$$\left.\begin{aligned} \frac{\partial(v+fx)}{\partial x}+\frac{\theta_c^2 N^2 f\gamma}{g^2}\frac{\partial\Pi}{\partial\theta}=0, \\ \frac{\partial(v+fx)}{\partial\theta}-\frac{1}{f}\frac{\partial\Pi}{\partial x}=0, \end{aligned}\right\} \quad \text{if } \varrho<\varrho_0,$$

$$\left.\begin{aligned} \frac{\partial(v+fx)}{\partial\varrho}+\frac{\theta_c N}{g}\frac{\partial\Pi}{\partial\varphi}=0, \\ \frac{\partial(v+fx)}{\partial\varphi}-\frac{\theta_c N}{g}\frac{\partial\Pi}{\partial\varrho}=0, \end{aligned}\right\} \quad \text{if } \varrho>\varrho_0, \tag{14}$$

$$v \to 0 \quad \text{and} \quad \Pi \to \tilde{\Pi} \quad \text{as} \quad \varrho \to \infty,$$
$$v \text{ and } \Pi \text{ continuous across } \varrho=\varrho_0.$$

The validity of equation (14) in the region $\varrho > \varrho_0$ can be confirmed by forming $(\partial x/\partial\varrho)\cdot(7)+(\partial\theta/\partial\varrho)\cdot(8)$ and using $(\partial x/\partial\varrho)=[g/(\theta_c N f)](\partial\theta/\partial\varphi)$ and then forming $(\partial x/\partial\varphi)\cdot(7)+(\partial\theta/\partial\varphi)\cdot(8)$ and using $(\partial x/\partial\varphi)=-[g/(\theta_c N f)](\partial\theta/\partial\varrho)$. The final solutions for v and Π are obtained by solving equation (14) inside ($\varrho<\varrho_0$) and outside ($\varrho>\varrho_0$) the PV anomaly and then requiring v and Π to be continuous along the ellipse $\varrho=\varrho_0$. As is easily confirmed by direct substitution, the solutions are

$$v(x,\theta)=\frac{f(\gamma-1)b}{\gamma a+b}\begin{cases} x & \text{if } \varrho \le \varrho_0 \\ ae^{\varrho_0-\varrho}\cos\varphi & \text{if } \varrho \ge \varrho_0, \end{cases} \tag{15}$$

$$\Pi(x,\theta)=\tilde{\Pi}(\theta)+\frac{g f(\gamma-1)a}{\theta_c N(\gamma a+b)}\begin{cases} \dfrac{g(\theta-\theta_c)}{(\theta_c N f)} & \text{if } \varrho \le \varrho_0 \\ be^{\varrho_0-\varrho}\sin\varphi & \text{if } \varrho \ge \varrho_0. \end{cases} \tag{16}$$

Since the terms in the second lines of equations (15) and (16) decay exponentially with ϱ, the far-field boundary conditions are satisfied. As is easily checked, the v field, given by equation (15), and the Π field, given by equation (16), are continuous at $\varrho=\varrho_0$. Thus, equations (15) and (16) are the desired solutions satisfying the boundary and interface conditions. Note that we have chosen to express the solutions in terms of the independent variables (x,θ) inside the PV anomaly and in terms of the independent variables (ϱ,φ) outside the PV anomaly. Of course, it is possible to express the solutions entirely in terms of (x,θ) or entirely in terms of (ϱ,φ), but such formulas are less compact than the mixed forms (15) and (16).

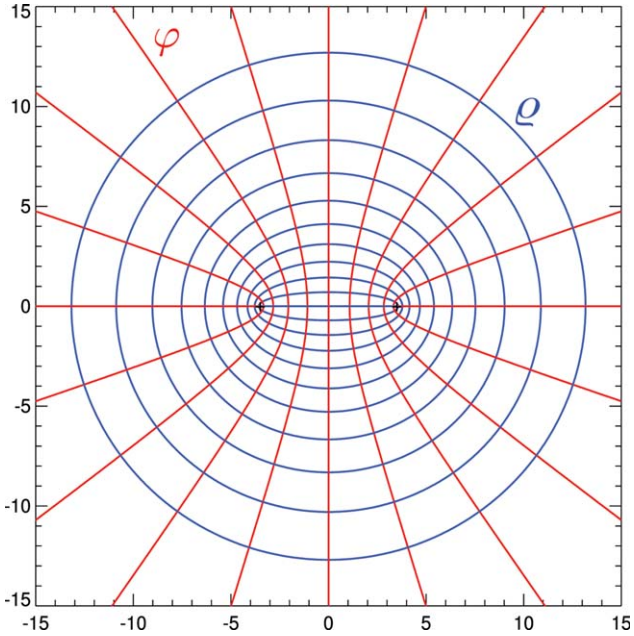

Figure 4. Elliptic coordinates (ϱ,φ), as defined in equation (10) for the thin lens case $(a > b)$. The horizontal axis is x and the vertical axis is $g(\theta-\theta_c)/(\theta_c N f)$, with both axes labeled in kilometers. Lines of constant ϱ (blue) are ellipses, and lines of constant φ (red) are hyperbolas. Both sets of curves have the same foci, located at $(x,\theta)=(\pm c,\theta_c)$. Far from the origin, lines of constant ϱ are very nearly circles, and lines of constant φ are very nearly straight radials. The 20 selected values of φ are 0°, 18°, 36°, … 342°.

[10] As an example, Figure 5 (top) shows the plots of equations (15) and (16) for $g=9.8$ m s^{-2}, $f=5\times10^{-5}$ s^{-1}, $N=1.03\times10^{-2}$ s^{-1}, $\theta_c=350$ K, $\Pi_c=c_p(p_c/p_0)^{\kappa}$, $p_c=200$ hPa, $a=500$ km, $b/a=2.30$, and $\gamma=8$. In the construction of Figure 5 (top), we have chosen to display isolines of v and Π (but labeled in terms of pressure) in (x,θ) space. Figure 5 (bottom) displays the same information, but now as isolines of v and θ in (x,p) space. Conversion from the top representation to the bottom representation has been accomplished by simple interpolation. The maximum value of the wind speed $v_{\max}$ occurs at the two points on the left and right edges of the elliptical PV anomaly, where $x=\pm a$ and $\theta=\theta_c$, or equivalently where $\varrho=\varrho_0$ and $\varphi=0,\pi$. At these points, equation (15) yields

$$v_{\max}=f b\left(\frac{|\gamma-1|}{\gamma+b/a}\right). \tag{17}$$

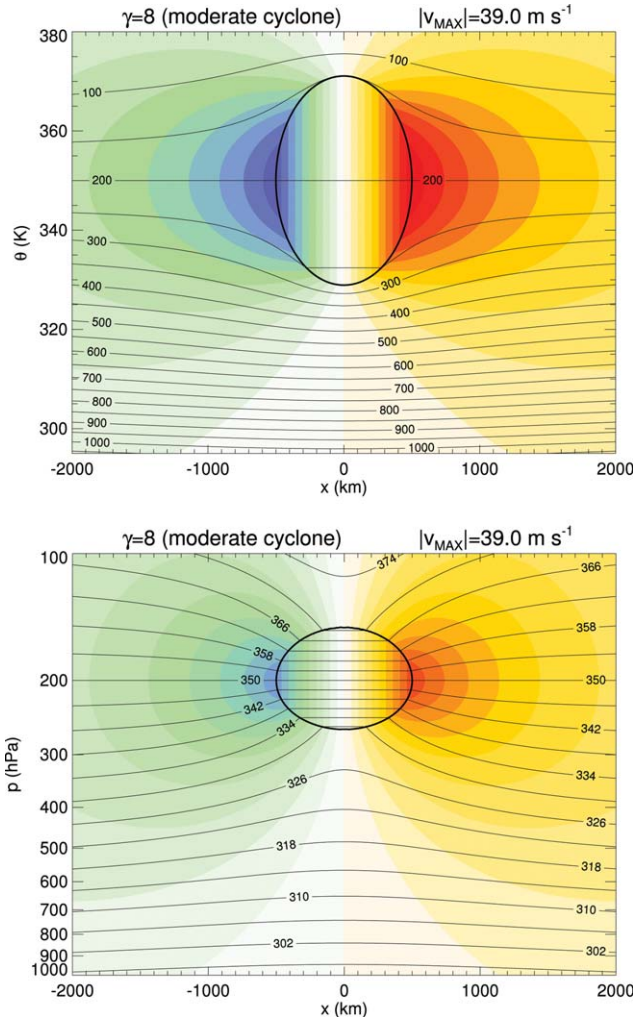

Figure 5. (top) Cross section of wind speed $v(x,\theta)$ and pressure $p(x,\theta)$ for a cyclone centered at $\theta=350$ K and the PV parameter $\gamma=8$. Wind speed (color) is contoured every 4 m s^{-1}, and pressure (lines) is contoured every 50 hPa. (bottom) Same information in the more conventional form $v(x,p)$ and $\theta(x,p)$, with the potential temperature values contoured every 4 K.

With the above choices of the constants f, a, b, and γ we obtain a maximum wind speed of $v_{\max}=39.0$ m s^{-1} at 200 hPa. Note that equation (17) implies that for large γ, the maximum wind speed is sensitive to the depth b of the PV anomaly.

[11] Figure 6 shows the plots of equations (15) and (16) for the same parameter values used in Figure 5, except with the six values of γ and b/a given in the first six rows of Table 1. The three examples of cyclones ($\gamma=4$, 8, 12) are shown on the left, while the three examples of anticyclones ($\gamma=1/4$, 1/8, 1/12) are shown on the right. Like PV itself, both $(\partial v/\partial x)$ and $(\partial\Pi/\partial\theta)$ are in general discontinuous across the ellipse. However, four locations on the ellipse are special. At $(\varrho,\varphi)=(\varrho_0,\pi/2)$ and $(\varrho,\varphi)=(\varrho_0,3\pi/2)$, we find that the vorticity is continuous, but the stability experiences its largest jump. Similarly, at $(\varrho,\varphi)=(\varrho_0,0)$ and $(\varrho,\varphi)=(\varrho_0,\pi)$, we find that the stability is continuous but the vorticity experiences its largest jump. The dashed lines in Figure 6 are lines along which $(\partial v/\partial x)=0$ and $(\partial\Pi/\partial\theta)=(\partial\tilde{\Pi}/\partial\theta)$. These four dashed lines divide the region outside the ellipse into four subregions. Above and below the ellipse, two subregions of enhanced vorticity and reduced stability fan out vertically, while to the left and right of the ellipse, two subregions of reduced vorticity and enhanced stability fan out horizontally.

[12] One reason that the solutions (15) and (16) have such a simple mathematical form is that N has been assumed to be a constant. However, for PV anomalies near the tropopause, the increased value of N in the stratosphere should be taken into account since it has an influence on the upward extension of the balanced wind and mass fields, as can be seen in the numerical results of *Hoskins et al.* [1985] and *Thorpe* [1986]. Their results clearly show that the high static stability of the stratosphere is associated with a locally reduced Rossby penetration depth, so that the influence of an upper tropospheric PV anomaly does not penetrate upward as far into the stratosphere as it would in the absence of enhanced stratospheric stability. This effect should be kept in mind when examining the idealized, constant N, analytical solutions presented here.

[13] The solutions (15) and (16) are useful for understanding how the PV is partitioned between vorticity and static stability. For example, by differentiation of equations (15) and (16) it can be shown that the dimensionless isentropic absolute vorticity is given by

$$\frac{f+(\partial v/\partial x)}{f}=\frac{1}{\gamma+b/a}\begin{cases}\gamma(1+b/a) & \text{if } \varrho<\varrho_0\\ \gamma+b/a+(\gamma-1)F & \text{if } \varrho>\varrho_0,\end{cases} \tag{18}$$

and the dimensionless (inverse) static stability by

$$\frac{(\partial\Pi/\partial\theta)}{(\partial\tilde{\Pi}/\partial\theta)}=\frac{1}{\gamma+b/a}\begin{cases}1+b/a & \text{if } \varrho<\varrho_0\\ \gamma+b/a+(\gamma-1)F & \text{if } \varrho>\varrho_0,\end{cases} \tag{19}$$

where

$$F(\varrho,\varphi)=e^{\varrho_0-\varrho}\begin{cases}\dfrac{b}{c}\left(\dfrac{\cosh\varrho\,\sin^2\varphi\,-\,\sinh\varrho\,\cos^2\varphi}{\cosh^2\varrho\,\sin^2\varphi\,+\,\sinh^2\varrho\,\cos^2\varphi}\right) & \text{if } a>b\\ \dfrac{b}{c}\left(\dfrac{\sinh\varrho\,\sin^2\varphi\,-\,\cosh\varrho\,\cos^2\varphi}{\sinh^2\varrho\,\sin^2\varphi\,+\,\cosh^2\varrho\,\cos^2\varphi}\right) & \text{if } a<b.\end{cases} \tag{20}$$

Note that equation (18) divided by equation (19) yields

$$\left(\frac{f+(\partial v/\partial x)}{f}\right)\left(\frac{\partial\tilde{\Pi}/\partial\theta}{\partial\Pi/\partial\theta}\right)=\begin{cases}\gamma & \text{if } \varrho<\varrho_0\\ 1 & \text{if } \varrho>\varrho_0,\end{cases} \tag{21}$$

which is the normalized version of equation (3). Using the top lines of equations (18) and (19) in equation (21),

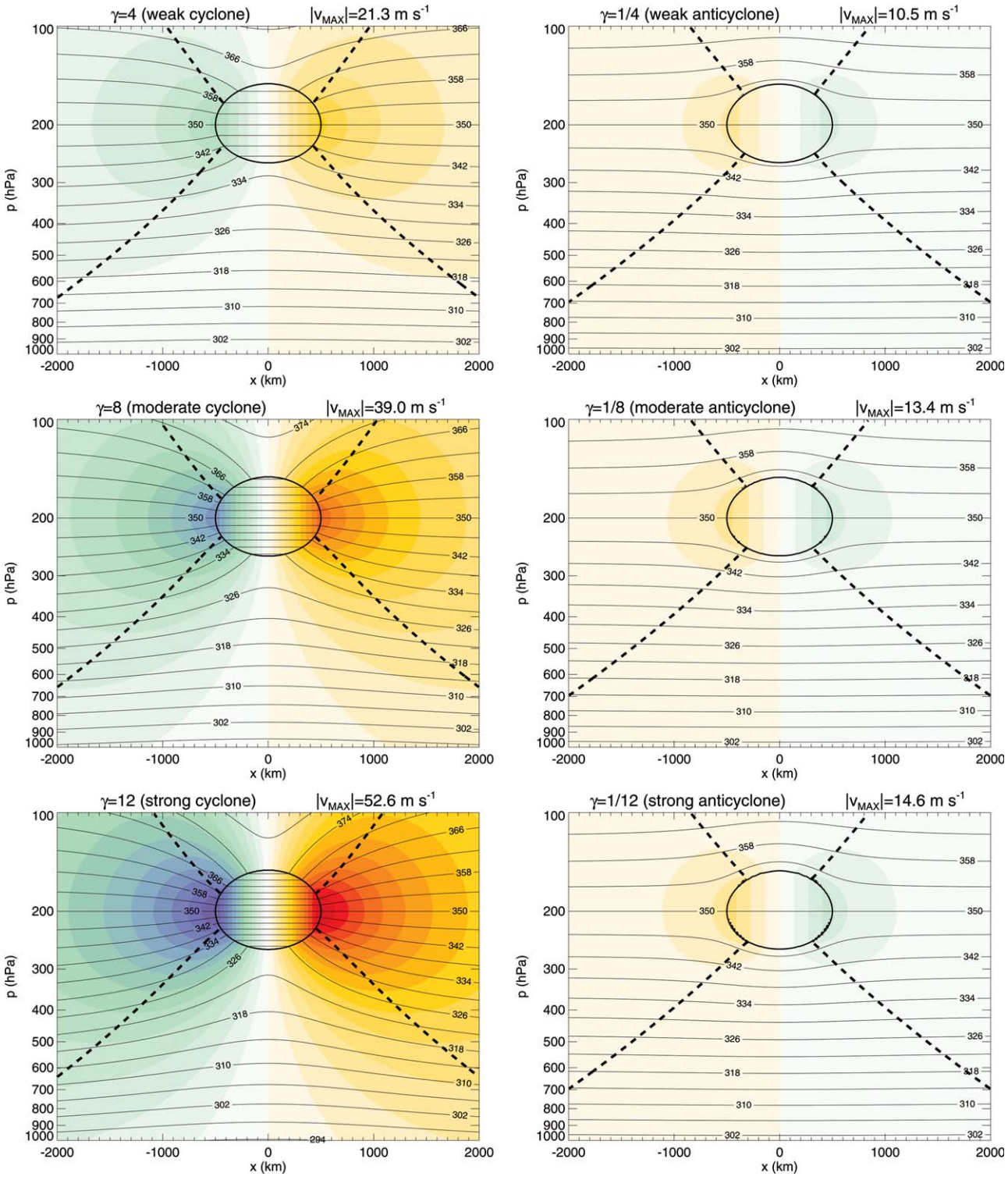

Figure 6. Cross-section plots of wind speed (v, colors) and potential temperature (θ, lines) for PV anomalies with six selected values of the PV parameter γ. Cyclones of increasing intensity are shown in the left column (γ=4, 8, 12), and anticyclones of increasing intensity are shown in the right column (γ=1/4, 1/8, 1/12). Wind speed values are contoured every 4 m s^{-1}, and potential temperature values are contoured every 4 K. The region of enhanced PV is outlined by the thick black ellipse, whose shape is defined by a=500 km and by the first six values of b/a given in Table 1.

Table 1. Test Cases of Cyclonic and Anticyclonic PV Anomalies[a]

γ	b/a	v_{max} (m s^{-1})	$\left(\frac{f+(\partial v/\partial x)}{f}\right)\left(\frac{\partial\tilde{\Pi}/\partial\theta}{\partial\Pi/\partial\theta}\right)=\gamma$	$\alpha(\gamma, b/a)$
12	2.84	52.6	$(3.11)(3.86)=(3.46)^2=12$	0.804
8	2.30	39.0	$(2.56)(3.12)=(2.83)^2=8$	0.820
4	1.59	21.3	$(1.85)(2.16)=(2.00)^2=4$	0.858
1/4	0.316	10.5	$(.581)(.430)=(.500)^2=1/4$	1.35
1/8	0.198	13.4	$(.463)(.270)=(.354)^2=1/8$	1.72
1/12	0.148	14.6	$(.413)(.202)=(.289)^2=1/12$	2.05
12	4.14	70.5	$(3.82)(3.141)=(3.46)^2=12$	1.22
8	3.41	52.3	$(3.09)(2.588)=(2.83)^2=8$	1.19
4	2.46	28.6	$(2.14)(1.867)=(2.00)^2=4$	1.15
1/4	0.754	14.1	$(.437)(0.572)=(.500)^2=1/4$	0.763
1/8	0.594	18.1	$(.277)(0.451)=(.354)^2=1/8$	0.614
1/12	0.526	19.8	$(.209)(0.399)=(.289)^2=1/12$	0.523

[a]Numerical values of the PV magnitude γ (first column), the shape b/a (second column), the maximum wind (third column), the PV partitioning (fourth column), and the values of $\alpha(\gamma, b/a)$ (fifth column) are tabulated. The values of v_{max} are determined from equation (17), the PV partitioning from equations (18) and (19), and the values of $\alpha(\gamma, b/a)$ from equation (22). Cyclones ($\gamma > 1$) range from the strongest (γ=12) to the weakest (γ=4), and anticyclones (γ<1) range from the weakest (γ=1/4) to the strongest (γ=1/12). The last six rows of the table correspond to the six squares in Figure 7, while the first six rows correspond to the six triangles in Figure 7 and to the solutions shown in Figure 6. Note that for each set of six rows, the different b/a values were chosen so that the resulting elliptical PV anomalies given by equation (9) were approximately the same shape and size in (x, p) coordinates.

we can easily see that within the ellipse the partitioning of the dimensionless PV between the absolute vorticity and the static stability is

$$\left(\frac{\gamma(1+b/a)}{\gamma+b/a}\right)\left(\frac{\gamma+b/a}{1+b/a}\right)=\gamma,$$

so that the partitioning depends only on γ and b/a. In this sense, all PV anomalies with the same γ and the same b/a are dynamically similar. For the example shown in Figure 5, γ=8 and b/a=2.30, so that the partitioning is $(2.56)(3.12)=(2.83)^2=8$, i.e., the PV inversion in this case is biased toward stability, with a dimensionless absolute vorticity of 2.56 and a dimensionless stability of 3.12, while an equipartition would result in both the dimensionless absolute vorticity and the dimensionless stability taking on the value 2.83.

[14] Another way to quantify the partitioning is through the ratio

$$\alpha(\gamma, b/a)=\frac{(f+\partial v/\partial x)/f}{(\partial\tilde{\Pi}/\partial\theta)/(\partial\Pi/\partial\theta)}=\frac{\gamma(1+b/a)^2}{(\gamma+b/a)^2}. \qquad (22)$$

Figure 7 shows the isolines of $\alpha(\gamma, b/a)$ as a function of γ and b/a. Cases with $\alpha > 1$ are vorticity biased, while cases with $\alpha < 1$ are stability biased. The six cases shown in Figure 6 and detailed in the first six rows of Table 1 are indicated by the six triangles in Figure 7. For these six cases, the cyclones are stability biased and the anticyclones are vorticity biased. The last six rows of Table 1 detail the six other cases indicated by the squares in Figure 7. For these six cases, the situation is reversed in the sense that the cyclones are vorticity biased and the anticyclones are stability biased. More extreme biasing, such as indicated by the cross and diamond symbols in Figure 7, seem possible, although it should be noted that the largest values of γ and b/a are associated with PV fields that are so intense and so deep (for typical values of a) that they can result in unrealistically strong winds.

[15] The results shown in Figure 6 are in general agreement with the observational results of *Kelley and Mock* [1982], *Whitfield and Lyons* [1992], and *Price and Vaughan* [1992], who have found that tropical upper tropospheric troughs are cold core cyclones confined to the layer between 100 and 700 hPa, whose typical horizontal scale is on the order of several hundred kilometers. The coldest temperature anomaly in the trough occurs near 300 hPa with the maximum cyclonic circulation near 200 hPa. Troughs typically last for less than 5 days but may, in some cases, persist for nearly 2 weeks. In addition, these systems often move to the southwest and are characterized by subsidence and minimum cloudiness in their northwest quadrant and ascent and maximum cloudiness in their southeast quadrant.

[16] A common feature of moisture plumes is the sharp edge of the cloud field on its northwest side. This is consistent with the moderate and strong cyclone cases shown in Figure 6 (left). Strong upgliding motions tend to occur on isentropic surfaces that intersect the lower half of the elliptically shaped PV anomaly. The upgliding motion ends abruptly where the isentropic surfaces become horizontal inside the PV anomaly. Thus, the sharp edge of the cloud field on its west side can be interpreted as the western extent of the isentropic upglide region and the eastern extent of the PV anomaly.

[17] The isentropic upglide cases shown in Figure 6 are examples of vertical p-velocities produced by inviscid adiabatic processes. Can such vertical velocities be as strong as those produced by deep convective heating in the Intertropical Convergence Zone (ITCZ)? In the strong cyclone case the isentropic upglide effect in the region just below the elliptical PV anomaly is approximately 100 hPa/1000 km. For a relative easterly flow of 10 m s^{-1}, this corresponds to 100 hPa/10^5 s, or an ascent rate of 116 hPa d^{-1}, a value approximately equal

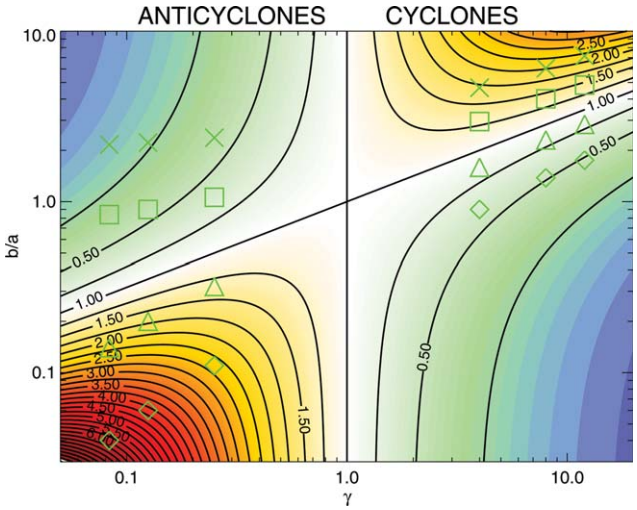

Figure 7. Isolines of $\alpha(\gamma, b/a)$, as defined in equation (22). PV inversion is vorticity biased for cases in which $\alpha>1$ (red/orange) and stability biased for cases in which $\alpha<1$ (blue/green). The six triangles correspond to the six cases detailed in the first six rows of Table 1 and shown in Figure 6, while the six squares correspond to the six cases detailed in the last six rows of Table 1.

to that observed in the western Pacific ITCZ [e.g., see *Yanai et al.*, 1973, Figure 3]. In addition, as discussed by *Hoskins et al.* [1985], there are two types of isentropic upglide: the first due to easterly relative flow below and east of an upper tropospheric PV anomaly; and the second due to southerly flow up an isentropic surface on the east side of the PV anomaly. The upglide by the second process can often be more important because of strong southerly flow and a long fetch along an isentropic surface that tilts upward toward the pole.

[18] In concluding this section we note that an interesting special case occurs when $\gamma \to 0$, which means that the PV is zero inside the ellipse. Equations (15) and (16) then reduce to

$$v(x,\theta) = -f \begin{cases} x & \text{if } \varrho \le \varrho_0 \\ a e^{\varrho_0 - \varrho} \cos\varphi & \text{if } \varrho \ge \varrho_0, \end{cases} \tag{23}$$

$$\Pi(x,\theta) = \tilde{\Pi}(\theta) - \frac{gfa}{\theta_c N} \begin{cases} \dfrac{g(\theta-\theta_c)}{\theta_c N f b} & \text{if } \varrho \le \varrho_0 \\ e^{\varrho_0 - \varrho} \sin\varphi & \text{if } \varrho \ge \varrho_0. \end{cases} \tag{24}$$

Note from equation (23) that the isentropic absolute vorticity $f+(\partial v/\partial x)$ vanishes in the ellipse. Also note from equation (24) that $(\partial\Pi/\partial\theta) = [1+(a/b)](\partial\tilde{\Pi}/\partial\theta)$. This zero PV case, described by equations (23) and (24), is similar in certain respects to the homogeneous intrusion case of *Gill* [1981], who studied the final geostrophically adjusted flow that occurs after a finite volume of constant temperature water is intruded into a uniformly rotating stratified ocean. This theoretical problem was motivated by the fortuitous discovery of Mediterranean eddies (or Meddies), as originally described by *McDowell and Rossby* [1978] and later reinterpreted by *Prater and Rossby* [2000]. However, it should be noted that the zero PV solution described here has nonvanishing stability and vanishing isentropic absolute vorticity, while Gill's zero PV solution has vanishing stability and nonvanishing isentropic absolute vorticity.

4. Surface Gradients

[19] The discussion in section 3 concerns interior PV anomalies. However, the solutions (15) and (16) can also be interpreted in terms of surface-based massless layers of infinite PV. To see this, consider the case in which the center of the ellipse is placed at the surface (i.e., $\theta_c=300$K, $\Pi_c = c_p(p_c/p_0)^\kappa$, and $p_c=p_0=1000$ hPa), and the PV inside the ellipse is allowed to become very large (i.e., $\gamma \to \infty$). Equations (15) and (16) then reduce to

$$v(x,\theta) = f b \begin{cases} x/a & \text{if } \varrho \le \varrho_0 \\ e^{\varrho_0 - \varrho}\cos\varphi & \text{if } \varrho \ge \varrho_0, \end{cases} \tag{25}$$

$$\Pi(x,\theta) = \Pi_c - \frac{gf\,b}{\theta_c N} \begin{cases} 0 & \text{if } \varrho \le \varrho_0 \\ \dfrac{g(\theta-\theta_c)}{\theta_c N f b} - e^{\varrho_0 - \varrho} \sin\varphi & \text{if } \varrho \ge \varrho_0. \end{cases} \tag{26}$$

Note from equation (26) that Π and hence p are constant in the ellipse (the massless layer).

[20] Figure 8 (top) shows the isolines of $v(x,\theta)$ and $p(x,\theta)$, computed from equations (25) and (26) for the parameters $g=9.8$ m s^{-2}, $f=5\times10^{-5}$ s^{-1}, $N=1.03\times10^{-2}$ s^{-1}, $a=500$ km, and $b=634$ km, which correspond to a warm surface potential temperature anomaly of magnitude $\theta_c N f b/g=10$ K. Figure 8 (bottom) displays the same information but in the more conventional form $v(x,p)$ and $\theta(x,p)$. Note that the half-ellipse region in Figure 8 (top) is the massless layer and that it becomes infinitesimally thin in Figure 8 (bottom). For the chosen parameters, the peak wind anomaly is 31.7 m s^{-1}. The specified 10 K surface potential temperature anomaly allows for a rough comparison of the present analytical results with the numerical results shown in *Hoskins et al.* [1985, Figure 16a] and in *Thorpe* [1986, Figure 4]. The results are qualitatively similar but differ quantitatively in an expected way when one notes that the present analytical results are for line symmetry and geostrophic balance, while their numerical results are for circular symmetry and gradient balance.

5. Numerical Solutions

[21] When the invertibility principle is solved using finite difference methods, it is unnecessary to make the approximation $(\rho/\tilde{\rho})=1$. Thus, in order to analyze the errors associated with this approximation, we now solve a finite difference version of the invertibility problem

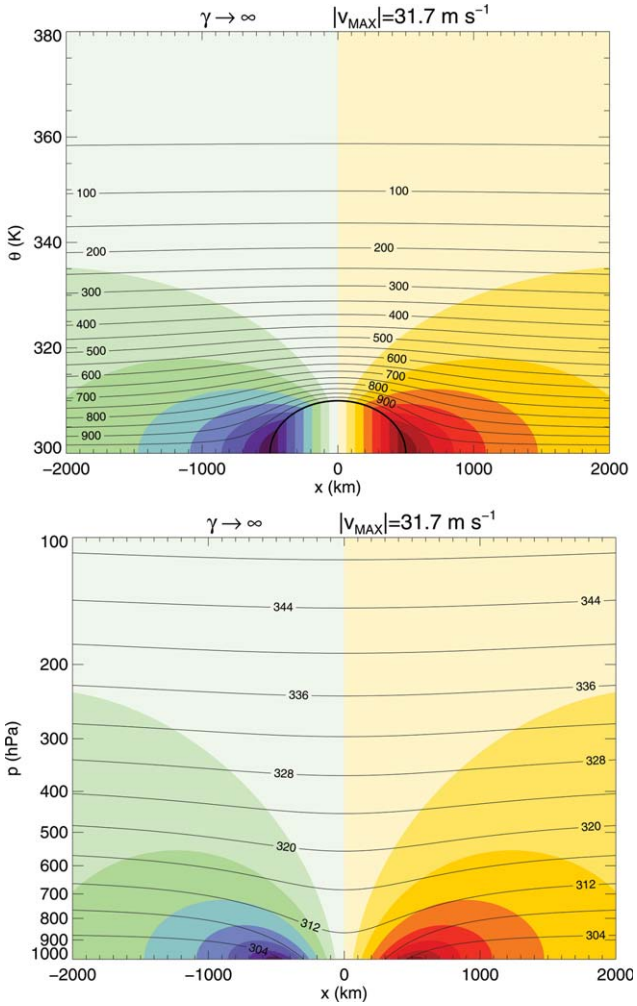

Figure 8. (top) Cross section of wind speed $v(x,\theta)$ and pressure $p(x,\theta)$ for a cyclone centered at the surface and for the PV parameter $\gamma\to\infty$. Wind speed (color) is contoured every 4 m s^{-1}, and pressure (lines) is contoured every 50 hPa. (bottom) Same information in the more conventional form $v(x,p)$ and $\theta\,(x,p)$, with the potential temperature values contoured every 4 K.

using an iterative method. Returning to equation (1) and making use of the geostrophic relation $fv=(\partial M/\partial x)$ and the hydrostatic relation $\Pi=(\partial M/\partial\theta)$, we obtain equation (27), where $M=\theta\Pi+\phi$ is the Montgomery potential, ϕ is the geopotential, and the density ρ is given in terms of M by equation (28). Note that the appearance of ρ (as opposed to $\tilde{\rho}$) in equation (27) retains the previously discussed weak nonlinearity, which is easily incorporated into the iterative method. To obtain the lateral boundary conditions (29) we have assumed that the far-field (i.e., $x=\pm L$) value of M is equal to the specified function $\tilde{M}(\theta)$. To obtain the upper boundary condition (30) we have assumed that the upper isentropic surface ($\theta=\theta_T$) is also an isobaric surface with a constant Exner function Π_T. To formulate the lower boundary condition (31) we have assumed that the geopotential vanishes along the lower isentropic surface, i.e., $M-\theta\Pi=0$ at $\theta=\theta_B$. In summary, the elliptic problem is

$$\frac{g}{f\theta\rho P}\left(f^2+\frac{\partial^2 M}{\partial x^2}\right)+\frac{\partial^2 M}{\partial\theta^2}=0, \tag{27}$$

$$\rho=\frac{p_0}{R\theta}\left(\frac{1}{c_p}\frac{\partial M}{\partial\theta}\right)^{(1-\kappa)/\kappa}, \tag{28}$$

$$M=\tilde{M}(\theta)\ \text{at}\ x=\pm L, \tag{29}$$

$$\frac{\partial M}{\partial\theta}=\Pi_T\ \text{at}\ \theta=\theta_T, \tag{30}$$

$$M-\theta\frac{\partial M}{\partial\theta}=0\ \text{at}\ \theta=\theta_B. \tag{31}$$

To solve equations (27)–(31) for $M(x,\theta)$, we must specify the constants θ_B, θ_T, Π_T, and L and the functions $P(x,\theta)$ and $\tilde{M}(\theta)$. In the following discussion we shall compare numerical solutions of equations (27)–(31) with numerical solutions of a system that is identical except that equation (28) is replaced by $\rho=\tilde{\rho}$. These comparisons will allow us to better understand the errors associated with the $(\rho/\tilde{\rho})=1$ approximation used in section 3.

[22] To discretize equation (27) we use centered finite difference approximations on the grid points $(x_j,\theta_k)=(-L+j\Delta x,\theta_B+k\Delta\theta)$ with $j=0,1,\ldots,J$ and $k=0,1,\ldots,K$, where $\Delta x=2L/J$ and $\Delta\theta=(\theta_T-\theta_B)/K$. We solve the discrete equations using the following successive overrelaxation (SOR) procedure. Denoting the current solution estimate by $M_{j,k}$ and sweeping through the grid in lexicographic order, we first compute the current estimate of density from

$$\rho_{j,k}=\frac{p_0}{R\theta_k}\left(\frac{M_{j,k+1}-M_{j,k-1}}{c_p 2\Delta\theta}\right)^{(1-\kappa)/\kappa}, \tag{32}$$

and then the current residual of equation (27) from

$$\begin{aligned} r_{j,k}=&M_{j,k-1}+M_{j,k+1}-2\left(1+A_{j,k}\right)M_{j,k}\\ &+A_{j,k}\left[(f\Delta x)^2+M_{j-1,k}+M_{j+1,k}\right], \end{aligned} \tag{33}$$

where

$$A_{j,k}=\frac{g(\Delta\theta)^2}{f\theta_k\rho_{j,k}P_{j,k}(\Delta x)^2}. \tag{34}$$

The solution estimate is then updated by

$$M_{j,k}\leftarrow M_{j,k}+\frac{\omega r_{j,k}}{2\left(1+A_{j,k}\right)}, \tag{35}$$

where ω is the overrelaxation factor, and equations (32)–(35) are computed at the grid points $1 \le j \le J-1, 1 \le k \le K-1$. Finally, the top and bottom boundary points are updated from the boundary conditions written in the form

$$M_{j,K} = M_{j,K-1} + \Pi_T \Delta\theta \qquad \text{for} \qquad 1 \le j \le J-1, \quad (36)$$

$$M_{j,0} = \left(\frac{\theta_B}{\theta_B + \Delta\theta}\right) M_{j,1} \qquad \text{for} \qquad 1 \le j \le J-1. \quad (37)$$

Equations (32)–(37) are iterated, starting with the initial estimate $M_{j,k} = \tilde{M}(\theta_k)$. This initial estimate does not change on the lateral boundaries $j=0$ and $j=J$.

[23] For the numerical solutions presented here, we have used the domain $-2000 \le x \le 2000$ km and $295 \le \theta \le 415$ K and a grid with $J=400$ and $K=300$, resulting in the grid spacing $\Delta x = 10$ km and $\Delta\theta = 120/300 = 0.4$ K. Note that equation (33) is isotropic on the grid if $A_{j,k}$ equals unity. Although such strict isotropy is obviously impossible, the pointwise SOR procedure works better if $\Delta\theta/\Delta x$ is chosen so that $A_{j,k}$ does not depart drastically from unity. Using typical values of the quantities on the right-hand side of equation (34), we find that our choice $(\Delta\theta/\Delta x) = (0.4\text{K})/(10\text{km})$ is reasonable in this regard.

[24] In order to gauge the convergence rate, we have monitored the norm of the residual as iteration proceeds. Experience shows that with the optimal value of the overrelaxation factor ω, this norm can be reduced by six or seven orders of magnitude in 1000 iterations, which is well beyond the accuracy required for present purposes. Based on the numerical tests, an overrelaxation factor of 1.98 has been used.

[25] In the analytical model of sections 3 and 4 the specified PV contains a discontinuity at the edge of the elliptically shaped anomaly. For the numerical solutions we modify this specification from equation (9) to

$$\frac{P}{\tilde{P}} = \begin{cases} \gamma & \text{if} \quad 0 \le \varrho \le \varrho_1, \\ \gamma S\left(\dfrac{\varrho - \varrho_1}{\varrho_2 - \varrho_1}\right) + S\left(\dfrac{\varrho_2 - \varrho}{\varrho_2 - \varrho_1}\right) & \text{if} \quad \varrho_1 \le \varrho \le \varrho_2, \\ 1 & \text{if} \quad \varrho_2 \le \varrho < \infty, \end{cases} \quad (38)$$

so that there is a smooth transition between the anomaly and the background field. In equation (38) the variable ϱ is the pseudo-radius of the elliptical coordinate system, and the smoothing function is defined by $S(s) = 1 - 3s^2 + 2s^3$. Note that $S(0)=1$ and $S(1)=0$, so that the middle line of equation (38) evaluates to γ when $\varrho = \varrho_1$, while it evaluates to 1 when $\varrho = \varrho_2$. The derivatives at these points are $S'(0)=0$ and $S'(1)=0$. From these considerations it is clear that between ϱ_1 and ϱ_2 the PV anomaly varies smoothly between γ and 1. In the limit $\varrho_1 \to \varrho_2$, definition (38) approaches definition (9).

[26] Figure 9 displays solutions to the problem (27)–(31) with P given by equation (38). These solutions are not directly comparable to those presented in Figure 6 for several reasons. First, the boundary conditions are different. While the effect of the localized PV anomaly simply decays with distance in the analytical model, the numerical model obeys the boundary conditions (29)–(31). Second, the density is approximated by the far-field density in the analytical model. In the numerical model we can work with either the unapproximated density $\rho(x,\theta)$ or the far-field density $\tilde{\rho}(\theta)$. Last, the smoothed PV anomaly (equation (38)) is slightly different than the discontinuous PV anomaly (equation (9)). The idea then is to compare the numerical solutions shown in Figure 9 with the density approximated numerical solutions. The numerical solutions with the density approximation $\rho = \tilde{\rho}$ are displayed in Figure 10. Comparing Figures 9 and 10, we see that the maximum wind speeds are very similar. For the cyclones, the density approximated solutions are slower, with this effect increasing as the intensity increases. The difference between the cyclones for $\gamma = 12$ is 3 m s^{-1}. For the anticyclones the density approximated solutions are faster. The difference in all the three cases is just 0.1 m s^{-1}.

[27] Qualitatively, the density approximated solutions (Figure 10) do not have the upward flare of the jets seen in the unapproximated solutions (Figure 9). The reason for this behavior can be deduced from Figures 11 and 12, which are the plots of the difference in density and the difference in wind speed, respectively, for a strong cyclone ($\gamma = 12$). Figure 11 shows that the density ρ is approximately 0.1 kg m^{-3} larger than $\tilde{\rho}$ in the upper half of the PV anomaly and is approximately 0.2 kg m^{-3} smaller than $\tilde{\rho}$ in the lower half of the PV anomaly. Looking at the difference of v in Figure 12 we see cyclonic flow in the upper region and anticyclonic flow in the lower region. Thus, the effect of using the actual density ρ instead of the approximate density $\tilde{\rho}$ is to shift the cyclonic circulation upward, creating the flare of the isotachs that is seen in Figure 9. For the anticyclone an analogous argument exists, and the anticyclonic circulation is seen to be shifted upward as well.

6. Concluding Remarks

[28] The main results of this work are the simple analytical solutions of the PV invertibility principle presented in sections 3 and 4. To obtain these solutions, isentropic coordinates were used to derive the Cauchy-Riemann equations for the case of line symmetric, geostrophic flow. The solutions describe the wind and mass fields both inside and outside a localized PV anomaly. The solutions are valid for equatorward intrusions of high PV as well as poleward intrusions of low PV. The case of high PV intruding into low latitudes is of most interest, due to the association with features in the cloud field (moisture bursts, cloud surges) and in the flow field (tropical upper tropospheric troughs), which have important implications for transient convection in the tropics as well as aiding in tropical cyclone development. Some essential characteristics of the solutions for high PV are the upgliding isentropes and cyclonic circulation. In the case of low PV intrusions the isentropes

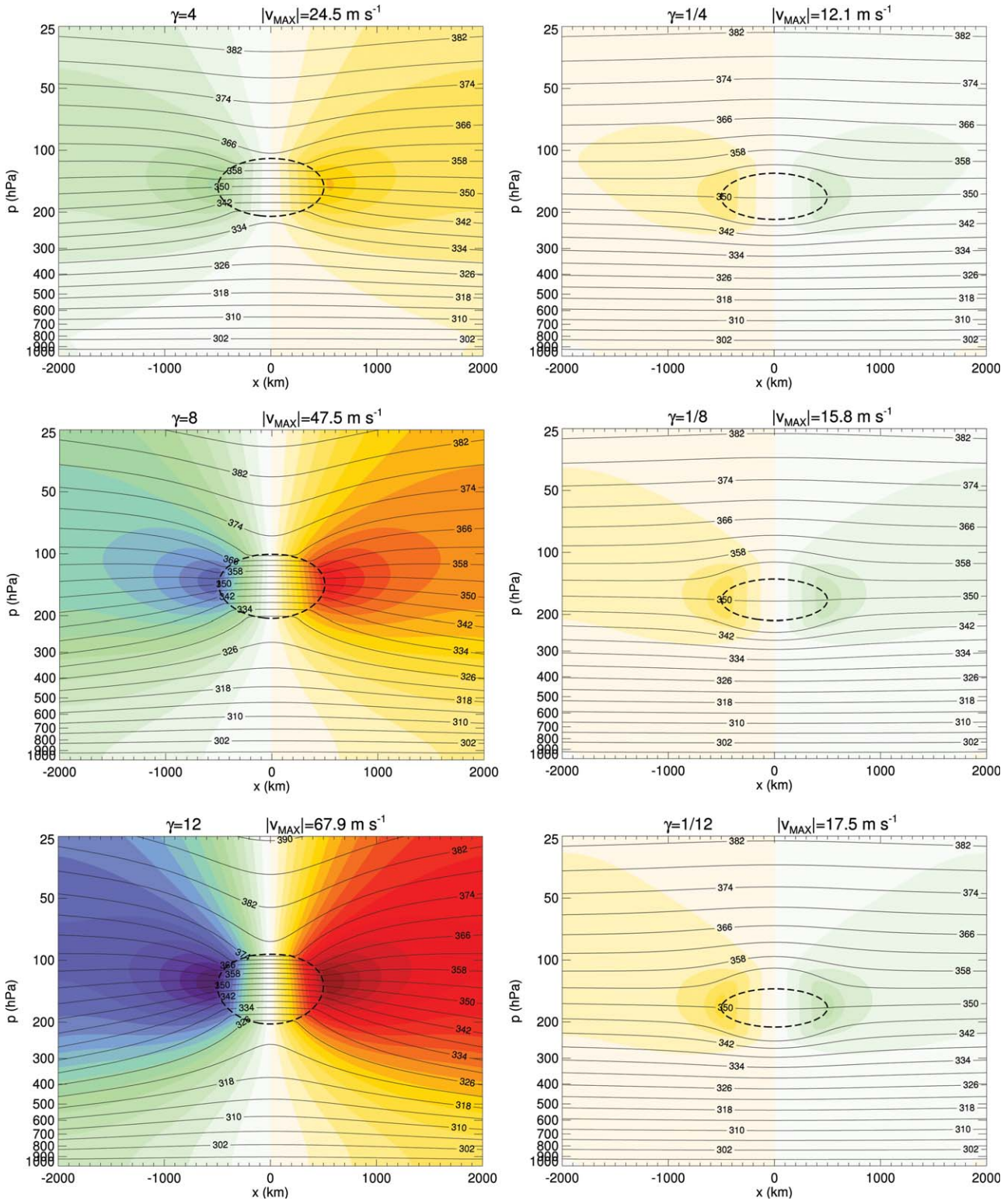

Figure 9. Cross-section plots of wind speed (v, colors) and potential temperature (θ, lines) for PV anomalies with select values of the parameter γ. Cyclones of increasing intensity are shown in the left column (γ=4, 8, 12), and anticyclones of increasing intensity are shown in the right column (γ=1/4, 1/8, 1/12). Wind speed values are contoured every 4 m s^{-1}, and potential temperature values are contoured every 4 K. The region of enhanced PV (see top line in equation (38)) is outlined by the dashed black ellipse, whose shape is defined by a=500 km and by the first six values of b/a given in Table 1.

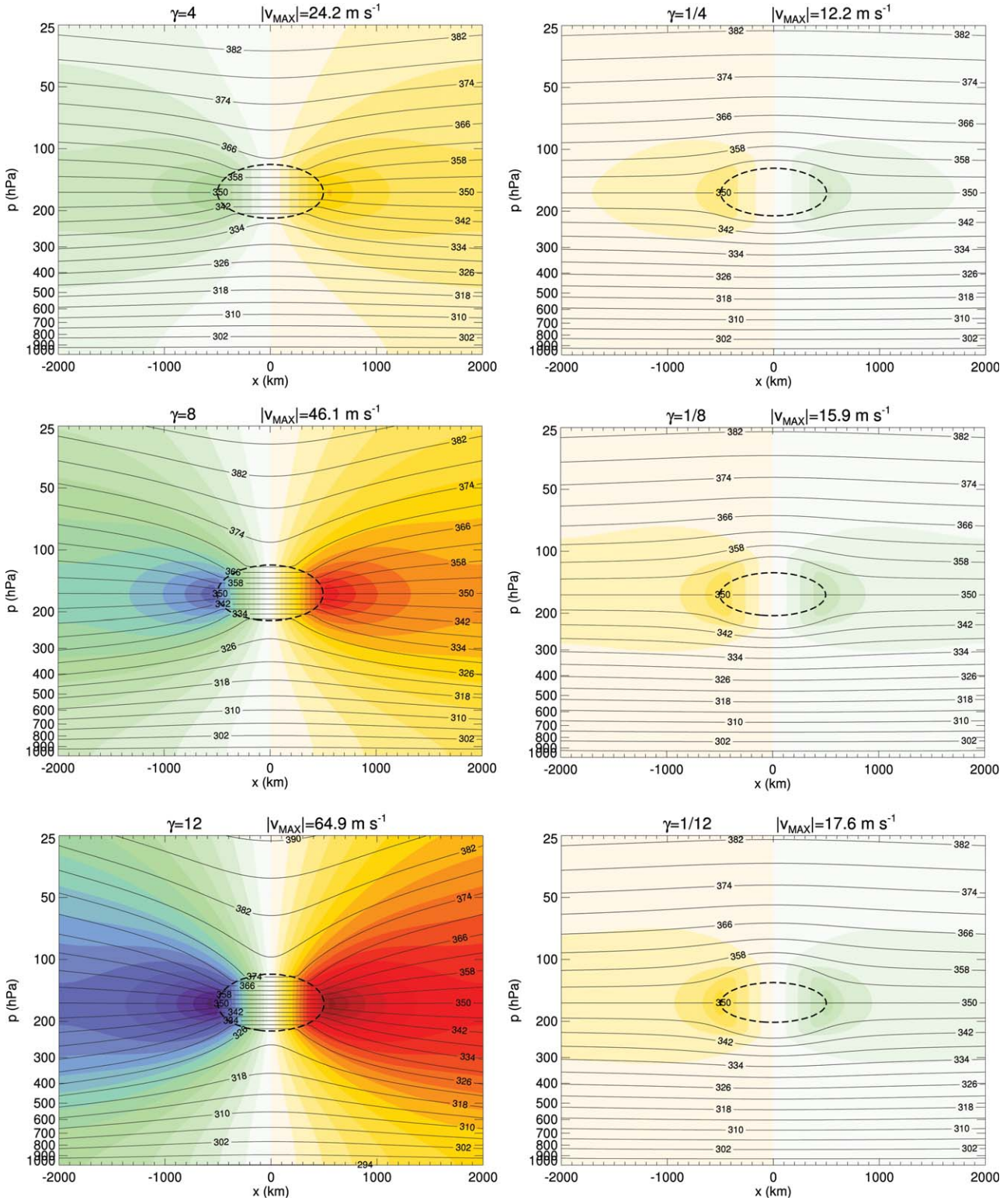

Figure 10. The conventions are the same as in Figure 9, though the density ρ, is set to the far-field value $\tilde{\rho}$.

were seen to bow outward from the PV anomaly, and the circulation was anticyclonic. By differentiating the solutions, analytical expressions can be obtained for the partitioning of PV anomalies between the absolute vorticity and the static stability. In the interior of the anomaly this partitioning is a function only of the aspect ratio (b/a) and the magnitude (γ). For cyclones, a deep PV lens is expressed as a vorticity-biased anomaly, and a shallow lens as a stability-biased anomaly. The opposite is true for an anticyclone.

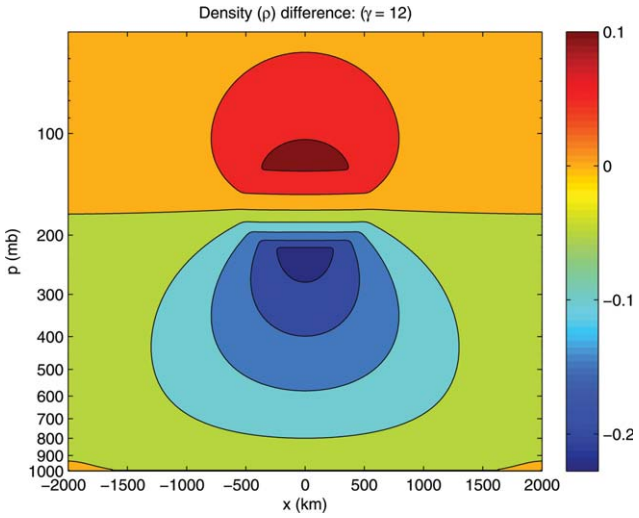

Figure 11. Contours of the density difference $\rho - \tilde{\rho}$ for the case of a strong cyclone (γ=12). The units are kg m^{-3}.

[29] In section 5, unapproximated versions of the equations used in the analytical theory were solved numerically. These numerical solutions provided a means to analyze the effect of approximating the density by the far-field density. When the density is not approximated, the equation set is weakly nonlinear, whereas the form used in the analytical theory is linear. In the numerical solutions the PV field is smoothed in the region between the ellipse of anomalous PV and the far-field. This smoothing aids the numerics but makes more difficult the task of comparing the numerical and analytical solutions. Because of this, as well as the use of different boundary conditions, we do not directly compare the numerical and analytical solutions.

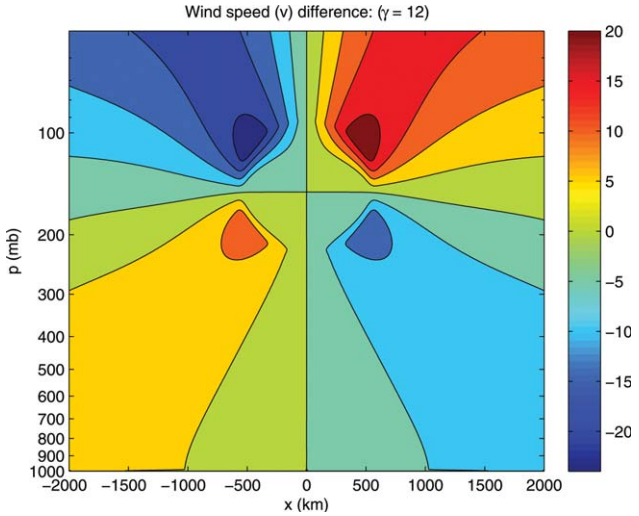

Figure 12. The difference of v (m s^{-1}), the v field with density approximated by the far-field density subtracted from the v field when density is unapproximated. For the case of a strong cyclone, γ=12.

Instead, we compare different numerical solutions for runs with the density approximated and runs with the density unapproximated. In terms of maximum wind speed, these solutions demonstrate that the density approximated cyclones are slightly slower. A qualitative comparison finds that the unapproximated solutions have a slight upward flare to the jets. This effect is due to the under(over)estimation of density in the upper (lower) region of the anomaly for the approximated case and acts to shift the circulation upward. Based on these small differences, we conclude that the analytical solutions are useful both qualitatively and semiquantitatively. With additional support from reanalysis data, the analytical model is found to be a useful theoretical tool for studying the flow field surrounding a PV intrusion.

[30] In the analysis presented here we have neglected the effects of topography and surface gradients of potential temperature. Recently, *Silvers and Schubert* [2012] have shown how these effects are crucial in understanding the low-level jets that are topographically bound to the Andes. Inclusion of topography and surface gradients of potential temperature in the present analysis would provide a framework for studying the flow fields that result when upper level and surface PV anomalies interact with elevated terrain. Such a combined model would be well suited to investigate the flows associated with atmospheric river events making landfall on western North America.

[31] In closing we note that the present analytical, line symmetric, geostrophic solutions of the PV invertibility principle provide a useful complement to the analytical, circularly symmetric, geostrophic solutions of *Eliassen and Kleinschmidt* [1957] and to the numerical, circularly symmetric, gradient solutions of *Hoskins et al.* [1985] and *Thorpe* [1986].

[32] **Acknowledgments.** We would like to thank Paul Ciesielski, Brian McNoldy, David Randall, Levi Silvers, and Rick Taft for their help and advice. This research has been supported by the National Science Foundation under grant ATM-0837932 and by the Science and Technology Center for Multi-Scale Modeling of Atmospheric Processes, managed by Colorado State University through cooperative agreement ATM-0425247. Workstation computing resources were provided through a gift from the Hewlett-Packard Corporation.

References

Appenzeller, C., and H. C. Davies (1992), Structure of stratospheric intrusions into the troposphere, *Nature*, *358*, 570–572.

Appenzeller, C., H. C. Davies, and W. A. Norton (1996), Fragmentation of stratospheric intrusions, *J. Geophys. Res.*, *101*, 1435–1456.

Dritschel, D. G. (1989), Contour dynamics and contour surgery: Numerical algorithms for extended, high-resolution modelling of vortex dynamics in two-dimensional, inviscid, incompressible flows, *Comput. Phys. Rep.*, *10*, 78–146.

Eliassen, A., and E. Kleinschmidt (1957), Dynamic meteorology, in: *Handbuch der Physik*, vol. 48, Geophysics II, S. Flügge (ed.), 154 pp., Springer-Verlag, Berlin.

Fueglistaler, S., A. E. Dessler, T. J. Dunkerton, I. Folkins, Q. Fu, and P. W. Mote (2009), Tropical tropopause layer, *Rev. Geophys.*, *47*, RG1004, doi:10.1029/2008RG000267.

Funatsu, B. M., and D. W. Waugh (2008), Connections between potential vorticity intrusions and convection in the eastern tropical Pacific, *J. Atmos. Sci.*, *65*, 987–1002.

Gettelman, A., and T. Birner (2007), Insights into tropical tropopause layer processes using global models, *J. Geophys. Res.*, *112*, D23104, doi:10.1029/2007JD008945.

Gettelman, A., et al. (2009), The tropical tropopause layer 1960–2100, *Atmos. Chem. Phys.*, *9*, 1621–1637.

Gill, A. E. (1981), Homogeneous intrusions in a rotating stratified fluid, *J. Fluid. Mech.*, *103*, 275–295.

Holton, J. R., P. H. Haynes, M. E. McIntyre, A. R. Douglass, R. B. Rood, and L. Pfister (1995), Stratosphere-troposphere exchange, *Rev. Geophys.*, *33*, 403–439.

Hoskins, B. J., and T. Ambrizzi (1993), Rossby wave propagation on a realistic longitudinally varying flow, *J. Atmos. Sci.*, *50*, 1611–1671.

Hoskins, B. J., M. E. McIntyre, and A. W. Robertson (1985), On the use and significance of isentropic potential vorticity maps, *Q. J. R. Meteorol. Soc.*, *111*, 877–946.

Hoskins, B. J., M. Pedder, and D. W. Jones (2003), The omega equation and potential vorticity, *Q. J. R. Meteorol. Soc.*, *129*, 3277–3303.

Iskenderian, H. (1995), A 10-year climatology of northern hemisphere tropical cloud plumes and their composite flow patterns, *J. Clim.*, *8*, 1630–1637.

Juckes, M. (1999), The structure of idealized upper-tropospheric shear lines, *J. Atmos. Sci.*, *56*, 2830–2845.

Juckes, M., and R. K. Smith (2000), Convective destabilization by upper-level troughs, *Q. J. R. Meteorol. Soc.*, *126*, 111–123.

Kelley, W. E., Jr., and D. R. Mock (1982), A diagnostic study of upper tropospheric cold lows over the Western North Pacific, *Mon. Weather Rev.*, *110*, 471–480.

Kiladis, G. N. (1998), Observations of Rossby waves linked to convection over the eastern tropical Pacific, *J. Atmos. Sci.*, *55*, 321–339.

Kiladis, G. N., and K. M. Weickmann (1992), Extratropical forcing of tropical Pacific convection during northern winter, *Mon. Weather Rev.*, *120*, 1924–1938.

Kley, D., H. G. J. Smit, S. Nawrath, Z. Luo, P. Nedelecand, and R. H. Johnson (2007), Tropical Atlantic convection as revealed by ozone and relative humidity measurements, *J. Geophys. Res.*, *112*, D23109, doi:10.1029/2007JD008599.

Masarik, M. T. (2012), Simple analytical solutions for potential vorticity intrusions, Ph.D. dissertation, 56 pp., Dep. of Atmos. Sci., Colo. State Univ., Fort Collins, Colo.

McDowell, S. E., and H. T. Rossby (1978), Mediterranean water: An intense mesoscale eddy off the Bahamas, *Science*, *202*, 1085–1087.

Postel, G. A., and M. H. Hitchman (1999), A climatology of Rossby wave breaking along the subtropical tropopause, *J. Atmos. Sci.*, *56*, 359–373.

Prater, M. D., and H. T. Rossby (2000), The double irony of the Meddy. Maritimes (Univ. Rhode Island Mar. Programs), *42*(3), 1–4.

Price, J. D., and G. Vaughan (1992), Statistical studies of cut-off-low systems, *Ann. Geophys.*, *10*, 96–102.

Scott, R. K., J.-P. Cammas, P. Mascart, and C. Stolle (2001), Stratospheric filamentation into the upper tropical troposphere, *J. Geophys. Res.*, *106*, 11,835–11,848.

Scott, R. K., D. G. Dritschel, L. M. Polvani and D. W. Waugh (2004), Enhancement of Rossby wave breaking by steep potential vorticity gradients in the winter stratosphere, *J. Atmos. Sci.*, *61*, 904–918.

Silvers, L. G., and W. H. Schubert (2012), A theory of topographically bound balanced motions and application to atmospheric low-level jets, *J. Atmos. Sci.*, *69*, 2878–2891.

Thorpe, A. J. (1986), Synoptic scale disturbances with circular symmetry, *Mon. Weather Rev.*, *114*, 1384–1389.

Tomas, R., and P. J. Webster (1994), Horizontal and vertical structure of cross-equatorial wave propagation, *J. Atmos. Sci.*, *51*, 1417–1430.

Waugh, D. W. (2005), Impact of potential vorticity intrusions on subtropical upper tropospheric humidity, *J. Geophys. Res.*, *110*, D11305, doi:10.1029/2004JD005664.

Waugh, D. W., and B. M. Funatsu (2003), Intrusions into the tropical upper troposphere: Three-dimensional structure and accompanying ozone and OLR distributions, *J. Atmos. Sci.*, *60*, 637–653.

Waugh, D. W., and L. M. Polvani (2000), Climatology of intrusions into the tropical upper troposphere, *Geophys. Res. Lett.*, *27*, 3857–3860.

Webster, P. J., and J. R. Holton (1982), Cross-equatorial response to middle-latitude forcing in a zonally varying basic state, *J. Atmos. Sci.*, *39*, 722–733.

Whitfield, M. B., and S. W. Lyons (1992), An upper-level low over Texas during summer, *Weather Forecasting*, *7*, 89–106.

Yanai, M., S. Esbensen, and J.-H. Chu (1973), Determination of bulk properties of tropical cloud clusters from large scale heat and moisture budgets, *J. Atmos. Sci.*, *30*, 611–627.

Corresponding author: W. H. Schubert, Department of Atmospheric Science, Colorado State University, Fort Collins, CO 80523-1371, USA. (waynes@atmos.colostate.edu)